Determination of ductile fracture parameters of a dual-phase steel by optical measurements

G. Gruben[a,*], D. Vysochinskiy[a], T. Coudert[b,a], A. Reyes[a] and O.-G.Lademo[b,a]

[a]Structural Impact Laboratory (SIMLab), Centre for Research-based Innovation (CRI) and Department of Structural Engineering, Norwegian University of Science and Technology, Rich. Birkelands vei 1A, NO-7491 Trondheim, Norway

[b]SINTEF Materials and Chemistry, Applied Mechanics and Corrosion, NO-7465 Trondheim, Norway

ABSTRACT: Marciniak-Kuczynski and Nakajima tests of the dual-phase steel Docol 600DL have been carried out for a range of stress states spanning from uniaxial tension to equi-biaxial tension. The deformation histories of the specimens have been recorded by digital images, and the displacement and strain fields have been determined by post-processing the images with digital image correlation software. The fracture characteristics of the material are presented by means of the stress triaxiality, the Lode parameter and the equivalent strain. These parameters are evaluated on the surface of the specimens based on the optical field measurements and assumptions regarding the mechanical behaviour of the material. Additionally the minor versus major principal strains up to fracture are presented. It is found that the material displays a significantly lower ductility in plane-strain tension than in uniaxial tension and equi-biaxial tension, and that it in the tests exposed to local necking undergoes large strains between the onset of necking and fracture. Fractographs of selected specimens reveal that fracture is due to growth and coalescence of voids that occur in localized areas governed by shear-band instability.

KEY WORDS: *Digital image correlation (DIC), dual-phase steel, ductile fracture, Lode parameter, stress triaxiality*

Introduction

Ductile fracture is controlled by nucleation, growth and coalescence of microvoids as explained by McClintock [1] and Rice and Tracey [2]. Increased hydrostatic pressure tends to decrease the rate of void growth, and so increase the ductility. The ductility can be expressed by the equivalent strain at fracture, $\bar{\varepsilon}_f = \bar{\varepsilon}(t_f)$, where t_f is the time at fracture and $\bar{\varepsilon}$ is the equivalent strain, defined as $\bar{\varepsilon} = \int_0^t \sqrt{2/3 \mathbf{D}:\mathbf{D}} \, dt$ where $\mathbf{D}$ is the rate-of-deformation tensor. A

commonly used parameter to describe the hydrostatic stress state is the stress triaxiality, σ^*, defined as

$$\sigma^* = \frac{\sigma_h}{\bar{\sigma}} \qquad (1)$$

where $\sigma_h = \text{tr}(\boldsymbol{\sigma})/3$ is the hydrostatic stress and $\bar{\sigma} = \sqrt{3/2\,\mathbf{s}:\mathbf{s}}$ is the von Mises equivalent stress with $\boldsymbol{\sigma}$ as the Cauchy stress tensor and $\mathbf{s}$ as the stress deviator. Recent findings from macro-scale experiments e.g. [3-5] indicate that the deviatoric stress state also influences the ductility in the range of low stress triaxiality σ^*. The deviatoric stress state can be expressed by the Lode parameter, μ, defined as [6]

$$\mu = \frac{2\sigma_{II} - \sigma_I - \sigma_{III}}{\sigma_I - \sigma_{III}} \qquad (2)$$

where σ_i, $i = I, II, III$ are the principal stresses ordered so that $\sigma_I \geq \sigma_{II} \geq \sigma_{III}$.

The digital image correlation (DIC) technique [7] is used to measure the displacement fields on the surface of the specimen during mechanical testing. The measured displacement fields can, in combination with certain assumptions regarding the mechanical behaviour of the material, be used in determining material properties from experiments. DIC was applied by Wu et al. [8] to estimate the accumulated damage in a 15-5PH steel during plastic deformation. Kirugulige and Tippur [9] used DIC to determine the stress intensity factors of a foam material under dynamic loading, while Luo and Wang [10] used DIC in determining the stress intensity factors as well as the J-integral from compact tension shear specimens made of 2024-O aluminium. However, stress and strain histories from material tests are traditionally found from numerical simulations of the tests, e.g. [3, 11-15], or analytical models, e.g. [16-17].

Gruben et al. [18] carried out experiments in the low range of stress triaxiality on steel sheets of Docol 600DL, which included uniaxial tension, plane-strain tension and in-plane shear, as well as two types of modified Arcan tests. In that study a novel method for experimental determination of σ^* and μ based on optical measurements of the displacement fields was presented and applied on selected tests. The method was used to derive σ^* and μ as well as the equivalent strain, $\bar{\varepsilon}$. In addition, σ^*, μ and $\bar{\varepsilon}$ were derived from finite

2

element simulations, and it was found that the average values of the stress state parameters, $\sigma^{*}_{\mathrm{avg}}$, μ_{avg}, as well as the equivalent strain at fracture (from now on called fracture strain), $\overline{\varepsilon}_{f}$, extracted by the two approaches were in good agreement. It was further found from the finite element simulations that the equivalent strain and the stress triaxiality were larger in the centre than on the surface of the specimen in four out of five tests, and so fracture was more likely to initiate in the centre of the specimen in these tests. As the experimental method is restricted to the surface of the specimen, it was concluded that use of surface displacement fields to determine the fracture strain could be considered a conservative approach for these tests.

In the present study, the Marciniak-Kuczynski [19] and Nakajima [20] test set-ups, which traditionally are used to investigate the formability of sheet materials, are applied to determine the fracture characteristics of the Docol 600DL material, thus expanding the experimental database for this material. The material is from the same batch as in the previous study by Gruben et al. [18], and the experimental method introduced in [18] is applied here. In addition, the forming limit and the fracture limit for the two test set-ups are derived from the DIC measurements and presented. Further, the fracture surfaces of selected test specimens are studied in a scanning electron microscope (SEM). It is concluded that the ductility of the material is significantly lower for (in-plane) plane-strain tension than for uniaxial tension and equi-biaxial tension, and that the tests exhibiting local necking underwent significant straining between the onset of local necking and fracture. The fracture mechanism in the tests is governed by nucleation, growth and coalescence of microvoids that occur in shear bands.

Experiments

Material

The material is a dual-phase steel delivered as 2 mm thick sheets from Swedish Steel AB (SSAB). It can be characterized as a low-strength, high-hardening material where the nominal yield stress is reported from the manufacturer to be in the range 280-360 MPa and the nominal ultimate stress is reported to be between 600 MPa and 700 MPa [21]. Through heat treatment the material is given a two-phase structure of ferrite and martensite, in which the ferrite gives the formability features, while the martensite proportion determines the strength. The nominal chemical composition of the material is given in Table 1. A previous study has

shown that the material exhibits a nearly isotropic behaviour in terms of work hardening and plastic flow [18].

Experimental set-up and optical measuring procedure

The Marciniak-Kuczynski and Nakajima experiments were carried out in a Zwick/Roell BUP 600 test machine as depicted in Fig. 1(A). All experiments were carried out in room temperature under quasi-static loading conditions and displacement control. The punch velocity was 0.3 mm/s, and two duplicate tests were performed for each specimen geometry. For both tests, a sheet of the material was clamped between a die and a blank holder with a clamping force. The clamping force can be altered, and in order to avoid fracture in the clamping zone, some tests were carried out to determine a reasonable clamping force for the tests in this study. The appropriate clamping force may vary for a different material and sheet thickness.

Apart from the test set-up and the use of three-dimensional DIC, the approach to collect data from the optical measurements is the same as in [18]. The main aspects of the approach are repeated here for convenience. Before testing, one side of the specimen was spray-painted by a combination of black and white paint, obtaining a high-contrast speckle pattern to improve the optical measurements. Two Prosilica GC2450 cameras equipped with 50 mm Nikon lenses were attached above the specimens as shown in Fig. 1(A). The cameras were recording the experiments with a framing rate of 2 Hz. A zone of each image from the gauge area, Fig 1(B), were post-processed by the three-dimensional DIC software 7D [22] following the coordinates of nodes, initially lying in a square pattern with 0.77 mm distance between them, see Fig. 1(C). In order to calculate the strain fields, the post-processing function in 7D utilized bilinear triangular elements in deriving the displacement gradient, $\partial \mathbf{u} / \partial \mathbf{X}$, where $\mathbf{u}$ is the in-plane displacement vector and $\mathbf{X}$ is the material coordinates. The deformation gradient, $\mathbf{F} = \partial \mathbf{u} / \partial \mathbf{X} + \mathbf{I}$, where $\mathbf{I}$ is the second order identity tensor, was further calculated and used in establishing the right Green deformation tensor defined as $\mathbf{C} = \mathbf{F}^T \cdot \mathbf{F}$. Further, the in-plane principal stretches, λ_i, were calculated by solving the eigenvalue problem for $\mathbf{C}$, i.e. $(\lambda_i^2 \mathbf{I} - \mathbf{C}) \cdot \mathbf{n}_i = \mathbf{0}$, where $\mathbf{n}_i$, $i = 1, 2$ are the principal in-plane directions of $\mathbf{C}$. The in-plane logarithmic strains were then calculated as

$$\varepsilon_i = \ln(\lambda_i) \qquad (3)$$

Assuming incompressibility and that the through-thickness shear strains are negligible (i.e. the thickness direction is assumed to be a principal direction), the through-thickness strain was estimated as $\varepsilon_Z = -(\varepsilon_1 + \varepsilon_2)$. The effective logarithmic strain was then calculated by

$$\varepsilon_e = \sqrt{\frac{2}{3}\left(\varepsilon_1^2 + \varepsilon_2^2 + \varepsilon_Z^2\right)} \tag{4}$$

It was generally not possible to pinpoint the exact position of fracture initiation within the gauge area. The point with maximum value of ε_e calculated by 7D in the last image before fracture was thus chosen as the point for collecting the deformation data; this is illustrated in Fig. 1(D). The four nodes enclosing the point of fracture initiation cf. Fig. 1(C), constituted the bilinear element used in calculating the time-histories of the parameters used in evaluating the material. This was conducted through post-processing in a MATLAB [23] script. It was found that warping of this four-node element was negligible in all the tests, i.e. the out-of-plane displacement was neglected. From the spatial coordinates of the four nodes, $\mathbf{x}(t)$, the deformation gradient, $\mathbf{F}(t)$, was evaluated at the centre point of the element. In addition to calculating $\varepsilon_1, \varepsilon_2, \varepsilon_Z$ and ε_e following the same procedures as 7D, the objective principal strain increments were sought from the point of fracture initiation. The in-plane Green strain tensor, $\mathbf{E} = (\mathbf{F}^T \cdot \mathbf{F} - \mathbf{I})/2$, was evaluated, and the temporal increment of the in-plane Green strain tensor, $\Delta\mathbf{E} = (\mathbf{F}_{n+1}^T \cdot \mathbf{F}_{n+1} - \mathbf{F}_n^T \cdot \mathbf{F}_n)/2$, was derived. Here $\mathbf{F}_{n+1}$ and $\mathbf{F}_n$ are the deformation gradient at increment $n+1$ and n respectively. In order to obtain an objective in-plane strain-increment tensor, the push-forward operation was conducted on $\Delta\mathbf{E}$, that is; $\Delta t\mathbf{D} = \mathbf{F}_{n+1}^{-T} \cdot \Delta\mathbf{E} \cdot \mathbf{F}_{n+1}^{-1}$, where Δt is the time increment. The principal in-plane strain increments, $(\Delta\varepsilon_1, \Delta\varepsilon_2)$, were then calculated by solving the eigenvalue problem for the objective in-plane strain-increment tensor, i.e. $(\Delta\varepsilon_i\mathbf{I} - \Delta t\mathbf{D})\cdot\bar{\mathbf{n}}_i = \mathbf{0}$, where $\bar{\mathbf{n}}_i$, $i = 1,2$, are the corresponding direction vectors. The stress triaxiality and the equivalent strain were calculated under the assumption of plane stress, von Mises plastic flow potential, and neglecting the elastic strains. By defining the strain increment ratio as $\beta = \Delta\varepsilon_2 / \Delta\varepsilon_1$, these parameters are expressed as [18]

$$\sigma^* = \frac{\sqrt{3}}{3}\frac{\beta+1}{\sqrt{\beta^2 + \beta + 1}} \tag{5}$$

5

$$\bar{\varepsilon} = \sum \Delta \bar{\varepsilon} = \sum \sqrt{\frac{2}{3}(\Delta \varepsilon_1^2 + \Delta \varepsilon_2^2 + \Delta \varepsilon_Z^2)} \qquad (6)$$

where

$$\Delta \varepsilon_1 > 0, \qquad -2 < \beta \leq 1, \qquad \Delta \varepsilon_Z = -(\Delta \varepsilon_1 + \Delta \varepsilon_2) \qquad (7)$$

The last relation in Equation (7) is found by assuming incompressibility and that the thickness direction is a principal direction. A verification of the method is presented by Gruben in [24]. Smoothening was necessary in order to calculate σ^* and $\bar{\varepsilon}$. C^2 continuous cubic splines were fitted by the least squares method to the time histories of the nodal coordinates, $\mathbf{x}(t)$, enclosing the point of fracture initiation. The initial and final positions were used as boundary conditions on the smoothed curves. In the tests used in this study, 12 splines were found to be suitable. Fig. 2 shows the raw coordinates and the smoothed coordinates from one of the nodes enclosing the point of fracture initiation in one of the Nakajima tests (NK-8-2). For the history curve of σ^*, the same smoothening as used in [18] was applied for visualization purposes.

When calculating the logarithmic strains, $\varepsilon_1, \varepsilon_2, \varepsilon_Z$ and the effective logarithmic strain ε_e, smoothening was not used. However, in order to estimate the time at onset of local (or through-thickness) necking, the time derivative of the strain rate, $\dddot{\varepsilon}_e(t)$, was calculated. In this calculation, the smoothed time-histories of $\mathbf{x}(t)$ was used to derive $\varepsilon_e(t)$, and a direct numerical derivation was applied twice on $\varepsilon_e(t)$ to obtain $\ddot{\varepsilon}_e(t)$.

Marciniak-Kuczynski set-up

The Marciniak-Kuczynski (M-K) test set-up is illustrated in Fig. 3(A). The test specimens are rectangular plates with a length of 205 mm and varying widths of 155 mm, 160 mm, 165 mm and 205 mm, see Fig. 3(B). The specimens were labelled MK-XXX-Y, where XXX is the width of the specimen, and Y=1,2 is the duplicate number. A centring device, cf. Fig. 3(C), was used to lock the position of the specimen at the centre of the punch. To ensure that no tractions from the punch acted on the centre zone of the specimen, a friction sheet with the same width and length as the specimen and with a centred hole of 40 mm diameter was placed between the punch and the specimen. The friction sheet was 1.4 mm thick and made of a steel material with yield and ultimate stress around 185 MPa and 375 MPa, respectively. The

friction sheet was sand blasted on the side facing the specimen to increase the friction between the specimen and the friction sheet. This ensured that the friction sheet deformed together with the specimen. In order to reduce the strains in the specimen around the punch edges and make sure that fracture would occur at the centre of the specimen [25], a 0.1 mm thick layer of PTFE (Teflon) was placed between the punch and the friction plate, and the punch was lubricated with grease. The advantage of using a friction plate rather than a punch with a recess is the ability to perform the test with a regular flat punch, rather than a custom made part, as well as allowing easy adjustment of the radius of the hole if needed. The clamping forces used in the tests are listed in Table 2.

Nakajima set-up

The Nakajima test specimens consist of circular disks with eight various cut-outs. The specimens were labelled NK-X-Y, where X=1,2,..,8 is the test number and Y=1,2 is the duplicate number. Fig. 4(A) displays the specimen geometries. The specimens were cut as illustrated in Fig. 4(B) with 3 mm strips still attached to rectangular blanks, thus allowing the application of the same centring device used in the M-K tests to ensure proper position of the specimens. The Nakajima test set-up is displayed in Fig. 3(D). As can be seen, the Nakajima test set-up is similar to the M-K test set-up, but without the friction sheet and with a hemispherical punch rather than a flat punch. A 0.1 mm thick layer of Teflon was placed between the specimen and the punch to reduce friction. The clamping forces used in the Nakajima tests are listed in Table 2.

Results

Marciniak-Kuczynski tests

Three of the M-K set-ups are close to plane-strain tension (MK-155, MK-160 and MK-165), while the fourth is close to equi-biaxial tension (MK-205). Two of the test specimens did not fracture (MK-165-2 and MK-205-1) due to premature termination of the test. Fig. 5 shows the effective logarithmic strain field for the successful tests in the last image before fracture as well as the fractured specimens. The position at which deformation data were collected is indicated by arrows. The results in form of major vs. minor principal logarithmic strains and equivalent strain as function of stress triaxiality are shown in Fig. 6(A) and (B), respectively. As can be seen in Fig. 6(A), the MK-155 and MK-160 tests display very similar histories, while MK-165 starts out with a deformation unlike the other two, but ends up in plane-strain

deformation. These tests are exposed to local necking before fracture. The onset of local necking is marked with symbols for each test in Fig. 6(A). The method used to estimate the onset of local necking is described in the following 'Strain localization and fracture' section. It is noted that the material undergoes large strains in the time between onset of local necking and fracture. On the other hand, the MK-205 test is in a deformation state near equi-biaxial tension throughout the whole experiment and does not exhibit local necking before fracture. In Fig. 6(A), the positions of the forming limit curve and the fracture limit curve are indicated by dashed lines based on these tests. Fig. 6(B) shows that the fracture strain differs about 0.05 in the two set-ups where both duplicates were successful (MK-155 and MK-160). Notably, the test in equi-biaxial tension displays a significantly higher fracture strain than the other tests.

Nakajima tests

The stress state in the Nakajima tests varied between equi-biaxial tension for NK-1 to near uniaxial tension in NK-8. Two of the tests failed (NK-4-1 and NK-4-2) as fracture occurred in the clamping zone rather than in the gauge area. The effective logarithmic strain in the last image before fracture in each successful test is shown in Fig. 7. The major vs. minor principal logarithmic strains for all 14 successful tests are given in Fig. 8(A). As can be seen, the deformation state is very similar in both duplicate tests for each set-up. All tests except NK-8 (uniaxial tension), start out in equi-biaxial tension, before they move into their assumed "natural" stress state for a major principal strain of around 0.035. NK-8 starts out in near plane-strain tension before it changes over to uniaxial tension. The NK-1, NK-2 and NK-3 tests were not exposed to local necking before fracture, in contrast to NK-5, NK-6, NK-7 and NK-8. The onset of local necking is marked in Fig. 8(A), which also indicate the positions of the forming limit curve and the fracture limit curve based on these experiments. It is clear that also the Nakajima tests exposed to local necking display significant straining after the onset of local necking. Fig. 8(B) shows the fracture strain vs. stress triaxiality for all tests, and one can see that the fracture strain between duplicates is consistent for four of the specimen geometries. On the contrary, in the NK-1, NK-2 (equi-biaxial tension) and NK-6 (plane-strain tension) tests, the difference in fracture strain between the duplicates is somewhat larger. As in the M-K tests, high fracture strain in equi-biaxial tension and low fracture strain in plane-strain tension is observed.

Strain localization and fracture

Strain localization and fracture of the material in the investigated range of stress-states is examined by selecting a few tests that are subject to a closer study. The NK-8-2 test represents uniaxial tension, while the NK-5-1 and MK-155-1 tests represent plane-strain tension, and the NK-1-1 and MK-205-2 tests represent equi-biaxial tension. As indicated in Fig. 9(A), the Nakajima tests in uniaxial tension display a diffuse neck and a local neck before fracture. Fig. 9(B) and (D) show that the Nakajima and M-K tests in plane-strain tension display local necking, while Fig. 9(C) and (E) show that the equi-biaxial Nakajima and M-K tests do not exhibit local necking before fracture. Different methods have been used to determine forming limits from DIC measurements [26], and one promising method is the time-dependent method [27], which uses the time-derivative of the strain rate to determine the time of the onset of local necking. Fig. 10(A) displays the effective logarithmic strain as function of time, $\varepsilon_e(t)$, while Fig. 10(B) gives the time-derivative of the effective logarithmic strain-rate, $\ddot{\varepsilon}_e(t)$. Note that the nodal coordinates, $\mathbf{x}(t)$, have been smoothed for the calculation of $\ddot{\varepsilon}_e(t)$. As illustrated in Fig. 10(A), the NK-1-1 and MK-205-2 tests, which are in equi-biaxial tension, display a gradual increase in the strain rate. This stems from a nonlinear correlation between the applied displacement and the straining. From Fig. 10(B) it can be observed that only a small gradual increase in $\ddot{\varepsilon}_e(t)$ is present towards the end of the tests, which suggests that these tests do not exhibit local necking. The NK-8-2, NK-5-1 and MK-205-2 tests on the other hand, display an abrupt increase in $\ddot{\varepsilon}_e(t)$ before fracture, which can be interpreted as the onset of local necking, i.e. the forming limit. For both the Marciniak-Kuczynski and the Nakajima tests the time at the onset of local necking was qualitatively determined as the time when an abrupt increase in $\ddot{\varepsilon}_e(t)$ occurred for each case. This is illustrated by the MK-155-1, NK-5-1 and NK-8-2 tests in Fig. 10(B), where the assumed onset of local necking is marked.

Before final failure, shear-band instability occurred in all tests. This phenomenon occurred on a scale which is too small to be captured by the DIC technique with the resolution of the images used in this study. However, shear lips which typically follows shear-band localization [28], are present in all the fractured specimens. This is exemplified by the specimens displayed in Fig. 9. It is noted that the specimens in plane-strain tension display a

more rough fracture surface, as illustrated in Fig. 9(B) and (D), than the specimens in uniaxial or equi-biaxial tension.

The fracture surfaces of the five selected tests were further investigated in a scanning electron microscope of type Hitachi SU6600. Fig. 11(A-E) displays high magnification fractographs of the fracture initiation point in the Nakajima and M-K tests, while Fig. 11(F) displays the fracture surface of the NK-1-1 test at low magnification. It can be seen from Fig. 11(A-E) that the surface have small dimples, most of them $< 5\,\mu m$. This suggests that voids are nucleated at small particles that are closely spaced, and that the voids coalesce before they reach a larger size, leaving a macroscopically smooth surface typical for shear lips [28]. Three larger dimples with visible inclusions marked with an 'i' can be seen in Fig. 11(A-B) and (D). Areas with elongated dimples typical for shear fracture can be observed in Fig. 11(A-C). Some of these areas are marked with an 's'. An interesting observation in the NK-5-1, NK-1-1 and MK-205-2 tests is a groove located at the centre of the fracture surface. The groove, which is marked with a 'g', is illustrated in Fig. 11(F) at low magnification and in Fig. 11(B-C) and (E), at higher magnification. The groove might be a result of the concentrated deformation at the locus where the two shear bands meet.

Ductility as function of average hydrostatic and deviatoric stress state

As a complementary stress-state parameter to the stress triaxiality, the Lode parameter, μ, can be used to describe the deviatoric stress state of the material. For an in-plane isotropic material, under plane-stress conditions, it can be shown that the Lode parameter can be expressed as a function of stress triaxiality as

$$
\mu = \begin{cases}
\dfrac{-3}{9(\sigma^*)^2 - 1} \cdot \left(1 - \sqrt{12(\sigma^*)^2 - 27(\sigma^*)^4}\right) & \text{for} \quad \sigma_I = 0, \quad -\tfrac{2}{3} \le \sigma^* \le -\tfrac{1}{3} \\[2ex]
\sqrt{\dfrac{27(\sigma^*)^2}{4 - 9(\sigma^*)^2}} & \text{for} \quad \sigma_{II} = 0, \quad -\tfrac{1}{3} \le \sigma^* \le 0 \\[2ex]
-\sqrt{\dfrac{27(\sigma^*)^2}{4 - 9(\sigma^*)^2}} & \text{for} \quad \sigma_{II} = 0, \quad 0 \le \sigma^* \le \tfrac{1}{3} \\[2ex]
\dfrac{3}{9(\sigma^*)^2 - 1} \cdot \left(1 - \sqrt{12(\sigma^*)^2 - 27(\sigma^*)^4}\right) & \text{for} \quad \sigma_{III} = 0, \quad \tfrac{1}{3} \le \sigma^* \le \tfrac{2}{3}
\end{cases}
\tag{8}
$$

When the material is in a plane-stress condition, the Lode parameter does not provide more information about the stress-state due to the one-to-one relation between the Lode parameter

and the stress triaxiality. However, while the change in stress triaxiality is small when going from plane-strain tension ($\sigma^* \approx 0.58$) to equi-biaxial tension ($\sigma^* \approx 0.67$) the change in the deviatoric stress state is significant. This is captured by the Lode parameter which is zero in plane-strain tension and unity in equi-biaxial tension. Similarly the Lode parameter clearly distinguishes the uniaxial tension stress state by $\mu = 1$. Fig. 6(B) and Fig. 8(B) which gives $\bar{\varepsilon}$ as function of σ^* do not display the large change in the deviatoric stress state. In order to explicitly illustrate the effect of both the hydrostatic and deviatoric stress state on the fracture strain, data including the Lode parameter are given in this section and used in the subsequent discussion. Here, the average values of the stress triaxiality and the Lode parameter are used rather than the history curves. The average values are calculated by an integral expression over the equivalent strain as

$$\sigma_{\text{avg}}^* = \frac{1}{\bar{\varepsilon}_f} \int_0^{\bar{\varepsilon}_f} \sigma^*(\bar{\varepsilon}) d\bar{\varepsilon}, \qquad \mu_{\text{avg}} = \frac{1}{\bar{\varepsilon}_f} \int_0^{\bar{\varepsilon}_f} \mu(\bar{\varepsilon}) d\bar{\varepsilon} \qquad (9)$$

In order to facilitate the comparison of data from the different tests, the average values of the two duplicates for each test is presented. In the two M-K tests where only one duplicate was successful, the value from this test is presented. The results are compared to the data from [18] and given in Fig. 12 and Table 3. Fig. 12(A) displays the fracture strain as function of average stress triaxiality, while Fig. 12(B) gives the fracture strain as function of average Lode parameter. The plane-stress locus as defined by Equation (8), is compared to the parameters $(\sigma_{\text{avg}}^*, \mu_{\text{avg}})$ from the 16 tests in Fig. 12(C). It is noted that the deviation from the plane-stress locus in Fig. 12(C), most notably observed for the modified Arcan tests [18], stems from the averaging defined by Equation (9).

Discussion

From Fig. 12(A) it is seen that the tests in plane-strain tension display a drop in ductility compared to the tests in uniaxial tension and equi-biaxial tension. The low ductility in plane-strain tension is coherent with previous observations from experiments with thin-walled specimens on a martensitic boron steel by Mohr and Ebnoether [5] and on a TRIP780 steel by Dunand and Mohr [29]. Fig. 12(A) also shows that the shear test displays a somewhat larger fracture strain than the tests in uniaxial tension. The abrupt increase in ductility observed when going from plane-strain to equi-biaxial tension in Fig. 12(A) seems to be correlated with

the change in the deviatoric stress-state. This is illustrated by expressing the experimental data in the $\bar{\varepsilon}_f - \mu_{\mathrm{avg}}$ space, see Fig. 12(B), where a V-shaped pattern is observed for the tests with $\sigma^* > 1/3$. As can be seen in Fig. 12(B), there is a tendency for higher ductility in equi-biaxial tension, $\mu = +1$, than uniaxial tension $\mu = -1$. This is also in accordance with the observations in [5] and [29]. By inspecting Fig. 12(A) it can be seen that the Nakajima tests differ somewhat from the other tests in ductility for comparable stress triaxiality values. In uniaxial tension the fracture strain is lower than in the other tests, while in equi-biaxial tension the ductility is higher than in the other tests. The Nakajima tests are exposed to normal tractions as well as shear tractions on the side facing the punch; additionally the tests have a curvature in the gauge area. These differences may lead to the different results obtained from the Nakajima tests. Experimental scatter may also contribute. In terms of formability, it is known that different tests set-ups may lead to different results [30].

It is emphasised that the presented results of σ^* and μ is depending on an assumption of the plastic flow of the material, while the results in the $\varepsilon_1 - \varepsilon_2$ space does not depend on this assumption. In the calculation of σ^* and μ it is possible to assume a plastic flow potential that includes J_3 dependency, e.g. the high-exponent isotropic yield function proposed by Hershey [31], as well as account for through-thickness anisotropy, cf. Hosford and Caddell [32]. This would change the expression for the stress triaxiality in Equation (5), and the following output. However, Gruben et al. [18] found that a von Mises yield function with associated flow rule gave a good description of the material, thus the assumption of a von Mises flow potential was found suitable for this study. It is further stressed that the results presented in this paper are based on measurements conducted on the surface of the specimens, and that fracture may have initiated in the through-thickness centre of the specimens. Since the specimens are made of thin sheets, large differences in stress state through the thickness during deformation as well as fracture strain are not expected. The Nakajima tests are in this perspective most exposed to differences through the thickness. The determination of fracture parameters from the surface was considered conservative compared to the parameters extracted from the centre [18].

As pointed out above, fracture occurs due to the nucleation-growth-coalescence mechanisms in localized areas. In the literature several fracture criteria have been proposed that include this mechanism, most notably the Rice-Tracey criterion [2] which is uncoupled

with the constitutive relation and the Gurson criterion [33] which is coupled with the constitutive relation. Practically, these criteria gives predictions on the fracture strain that vary only with the stress triaxiality, and do not include the effect of the deviatoric stress-state. Thus, these criteria would not be able to predict the drop in ductility in plane-strain tension as observed in Fig. 12(A) and (B). Attempts have been made to include the effect of the deviatoric stress state in ductile fracture criteria. Examples of coupled approaches are e.g. the modified versions of the Gurson model presented by Xue [34] and Nahshon and Hutchinson [35]. In a parallel study [36], the modified Mohr-Coulomb criterion presented by Bai and Wierzbicki [37], and the extended Cockcroft-Latham and the extended Rice-Tracey criteria presented in [36] have been assessed for the Docol 600DL material. These three criteria are examples of uncoupled fracture criteria which explicitly takes into account the effect of the Lode parameter for low values of stress triaxiality.

Conclusions

In this study, two series of tests have been performed using Marciniak-Kuczynski and Nakajima test set-ups on 2 mm sheets of the dual-phase steel Docol 600DL. Displacement field data from the surface of the specimens obtained by digital image correlation have been used to determine the fracture strain of the material as function of stress triaxiality and Lode parameter. The results have been compared with results from a previous study on the same material with other material tests. The main finding is that the material displays a significant drop of ductility in the range of triaxiality around plane-strain tension, which was not captured by the tests conducted in the previous study. Further, it is found that the tests exposed to local necking undergo large strains between onset of local necking and fracture. The fracture mechanism in the tests is void growth and coalescence that mainly occurs in localized areas controlled by shear-band instability.

REFERENCES

1. McClintock, F.A. (1968) Criterion for ductile fracture by growth of holes. *J. Appl. Mech.* **35,** 363-371.
2. Rice, J.R. and Tracey, D.M. (1969) On the ductile enlargement of voids in triaxial stress fields. *J. Mech. Phys. Sol.* **17,** 201-217.
3. Bao, Y. and Wierzbicki, T. (2004) On fracture locus in the equivalent strain and stress triaxiality space. *Int. J. Mech. Sci.* **46,** 81-98.
4. Barsoum, I. and Faleskog, J. (2007) Rupture mechanisms in combined tension and shear—Experiments. *Int. J. Solids Struct.* **44,** 1768-1786.
5. Mohr, D. and Ebnoether, F. (2009) Plasticity and fracture of martensitic boron steel under plane stress conditions. *Int. J. Solids Struct.* **46,** 3535-3547.
6. Lode, W. (1926) Versuche über den Einfluß der mittleren Hauptspannung auf das Fließen der Metalle Eisen, Kupfer und Nickel. *Zeitschrift für Physik: A* **36,** 913-939.
7. Sutton, M.A., Mingqi, C., Peters, W.H., Chao, Y.J. and McNeill, S.R. (1986) Application of an optimized digital correlation method to planar deformation analysis. *Image and Vision Computing* **4,** 143-150.
8. Wu, T., Coret, M. and Combescure, A. (2011) Strain Localisation and Damage Measurement by Full 3D Digital Image Correlation: Application to 15-5PH Stainless Steel. *Strain* **47,** 49-61.
9. Kirugulige, M.S. and Tippur, H.V. (2009) Measurement of Fracture Parameters for a Mixed-Mode Crack Driven by Stress Waves using Image Correlation Technique and High-Speed Digital Photography. *Strain* **45,** 108-122.
10. Luo, P.F. and Wang, C.H. (2008) An Experimental Study on the Elastic–Plastic Fracture in a Ductile Material under Mixed-Mode Loading. *Strain* **44,** 223-230.
11. Wilkins, M.L., Streit, R.D. and Reaugh, J.E. (1980) *Cumulative-strain-damage model of ductile fracture: simulation and prediction of engineering fracture tests*. Technical Report UCRL-53058. Lawrence Livermore National Laboratory.
12. Hancock, J.W. and Brown, D.K. (1983) On the role of strain and stress state in ductile failure. *J. Mech. Phys. Sol.* **31,** 1-24.
13. Johnson, G.R. and Cook, W.H. (1985) Fracture characteristics of three metals subjected to various strains, strain rates, temperatures and pressures. *Eng. Fract. Mech.* **21,** 31-48.
14. Børvik, T., Hopperstad, O.S. and Berstad, T. (2003) On the influence of stress triaxiality and strain rate on the behaviour of a structural steel. Part II. Numerical study. *Eur. J. Mech. - A/Solids* **22,** 15-32.
15. El-Magd, E. and Abouridouane, M. (2006) Characterization, modelling and simulation of deformation and fracture behaviour of the light-weight wrought alloys under high strain rate loading. *International journal of impact engineering* **32,** 741-758.
16. Bridgman, P.W. (1952) *Studies in large plastic flow and fracture: with special emphasis on the effects of hydrostatic pressure* Harvard Univ. Press, Cambridge, Mass.
17. Hancock, J.W. and Mackenzie, A.C. (1976) On the mechanisms of ductile failure in high-strength steels subjected to multi-axial stress-states. *J. Mech. Phys. Sol.* **24,** 147-169.
18. Gruben, G., Fagerholt, E., Hopperstad, O.S. and Børvik, T. (2011) Fracture characteristics of a cold-rolled dual-phase steel *European Journal of Mechanics - A/Solids* **30,** 204-218.
19. Marciniak, Z. and Kuczyński, K. (1967) Limit strains in the processes of stretch-forming sheet metal. *Int. J. Mech. Sci.* **9,** 609-620.

20. ISO12004-2 (2008) *Metallic materials -Sheet and strip- Determination of forming-limit curves. Part 2: Determination of forming limit curves in the laboratory*. 1st edn.
21. SSAB (2009) Docol DP/DL Cold reduced dual phase steels.Swedish Steel AB. Accessed: 27.04.2012.
http://www.ssab.com/Global/DOCOL/datasheets_docol/en/201_Docol%20DP%20DL.pdf
22. Vacher, P., Dumoulin, S., Morestin, F. and Mguil-Touchal, S. (1999) Bidimensional strain measurement using digital images. *Journal of Mechanical Engineering Science* **213,** 811-817.
23. MATLAB (2009) version 7.9 (R2009b). The MathWorks Inc.
24. Gruben, G. (2012) Ductile fracture in dual-phase steel. Theoretical, experimental and numerical study. PhD thesis, Norwegian University of Science and Technology.
25. Hu, S.J., Marciniak, Z. and Duncan, J.L. (2002) *Mechanics of Sheet Metal Forming*. 2nd edn. Butterworth-Heinemann, Woburn.
26. Vysochinskiy, D., Coudert, T., Reyes, A. and Lademo, O.-G. (2012) Determination of forming limit strains using Marciniak-Kuczynski tests and automated digital image correlation procedures. Proc. ESAFORM 2012, Erlangen, Key Engineering Materials(504-506), 17-22.
27. Merklein, M., Kuppert, A. and Geiger, M. (2010) Time dependent determination of forming limit diagrams. *CIRP Annals - Manufacturing Technology* **59,** 295-298.
28. Anderson, T.L. (2005) *Fracture Mechanics; Fundamentals and Applications*. Third edn. Taylor & Francis Group, LLC, Boca Raton.
29. Dunand, M. and Mohr, D. (2010) Hybrid experimental-numerical analysis of basic ductile fracture experiments for sheet metals. *International Journal of Solids and Structures* **47,** 1130-1143.
30. Banabic, D. (2010) *Sheet Metal Forming Processes* Springer.
31. Hershey, A.V. (1954) The Plasticity of an Isotropic Aggregate of Anisotropic Face-Centered Cubic Crystals. *Journal Applied Mechanics* **76,** 241-249.
32. Hosford, W.F. and Caddell, R.M. (1993) *Metal Forming: Mechanics and Metallurgy*. 2nd edn. Prentice-Hall.
33. Gurson, A.L. (1977) Continuum theory of ductile rupture by void nucleation and growth, 1. Yield criteria and flow rules for porous ductile media. *J. Eng. Mat. Tech.*, 2-15.
34. Xue, L. (2008) Constitutive modeling of void shearing effect in ductile fracture of porous materials. *Eng Fract Mech* **75,** 3343-3366.
35. Nahshon, K. and Hutchinson, J.W. (2008) Modification of the Gurson Model for shear failure. *Eur J Mech A/Solids* **27,** 1-17.
36. Gruben, G., Hopperstad, O.S. and Børvik, T. (2012) Evaluation of uncoupled ductile fracture criteria for the dual-phase steel Docol 600DL. *Int. J. Mech. Sci.* **62,** 133-146.
37. Bai, Y. and Wierzbicki, T. (2010) Application of extended Mohr–Coulomb criterion to ductile fracture. *Int. J. Fract.* **161,** 1-20.

Table 1   Chemical composition of Docol 600DL (in wt %) [21].

C	Si	Mn	P	S	Al$_{tot}$
0.10	0.40	1.50	0.010	0.002	0.040

Table 2   Clamping force in the various tests.

Test	Test name	Duplicate number	Clamping force [kN]	Note
Marciniak-Kuczynski	MK-155	1	388.2	
		2	400.0	
	MK-160	1	391.4	
		2	391.4	
	MK-165	1	386.7	
		2	467.4	Failed
	MK-205	1	394.9	Failed
		2	401.4	
Nakajima	NK-1	1	400.4	
		2	399.1	
	NK-2	1	399.2	
		2	418.1	
	NK-3	1	397.4	
		2	400.3	
	NK-4	1	400.0	Failed
		2	300.0	Failed
	NK-5	1	271.5	
		2	272.5	
	NK-6	1	240.8	
		2	260.6	
	NK-7	1	216.5	
		2	229.1	
	NK-8	1	198.6	
		2	201.7	

Table 3   Fracture characteristics data for Docol 600DL steel.

Test name	σ^*_{avg}	μ_{avg}	$\overline{\varepsilon}_f$
Uniaxial tension [18]	0.427	-0.631	0.818
Plane-strain tension [18]	0.542	-0.167	0.682
In-plane shear [18]	0.005	-0.013	0.940
Arcan-45 [18]	0.311	-0.836	0.821
Arcan-90 [18]	-0.415	0.637	0.848
MK-155	0.576	-0.004	0.521
MK-160	0.586	0.049	0.505
MK-165	0.601	0.143	0.481
MK-205	0.666	0.911	0.851
NK-1	0.663	0.8359	1.041
NK-2	0.664	0.870	1.007
NK-3	0.658	0.667	0.791
NK-5	0.585	0.069	0.498
NK-6	0.530	-0.192	0.667
NK-7	0.463	-0.474	0.660
NK-8	0.429	-0.595	0.719
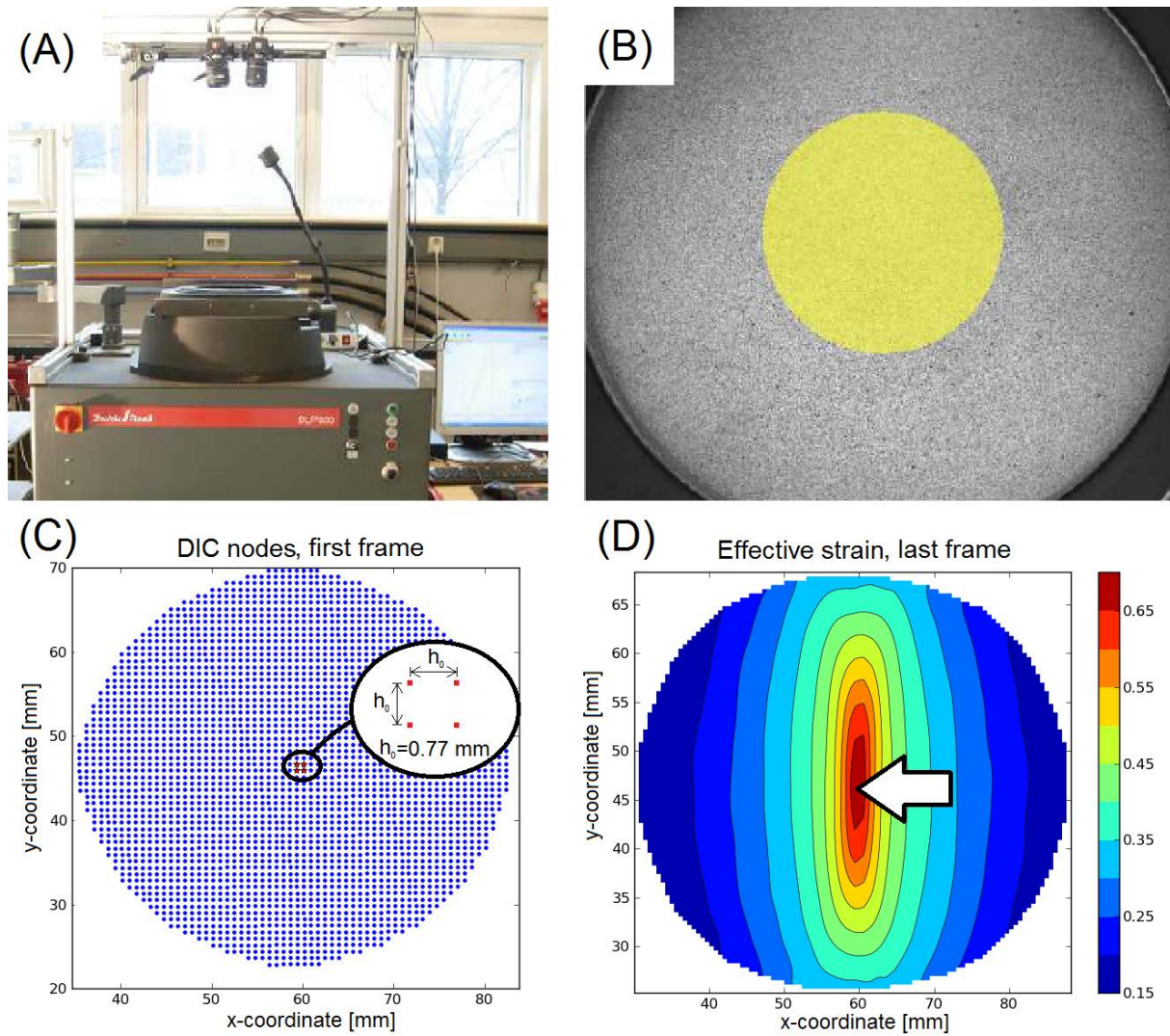
Fig. 1 (A) The Zwick/Roell BUP 600 test machine with two cameras for DIC measurements and (B) specimen with speckle pattern and zone (in yellow) for DIC measurement. (C) DIC nodes in the first image. The nodes constituting the element used for collecting fracture parameters are marked. (D) Effective strain in the last frame before fracture. The arrow points at the element used for collecting fracture data.
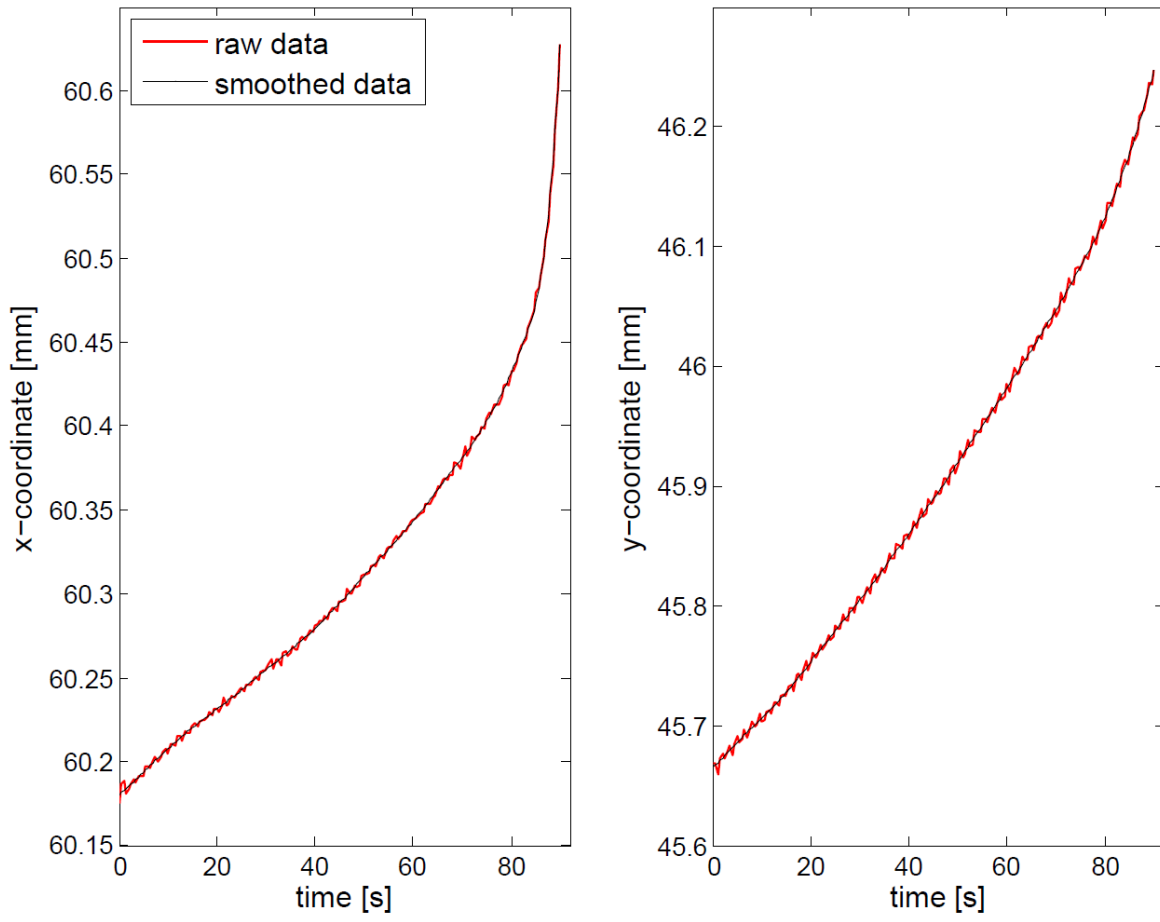
Fig. 2 Raw data and smoothed data of nodal coordinates from one of the nodes enclosing the point of fracture initiation in the Nakajima test NK-8-2.
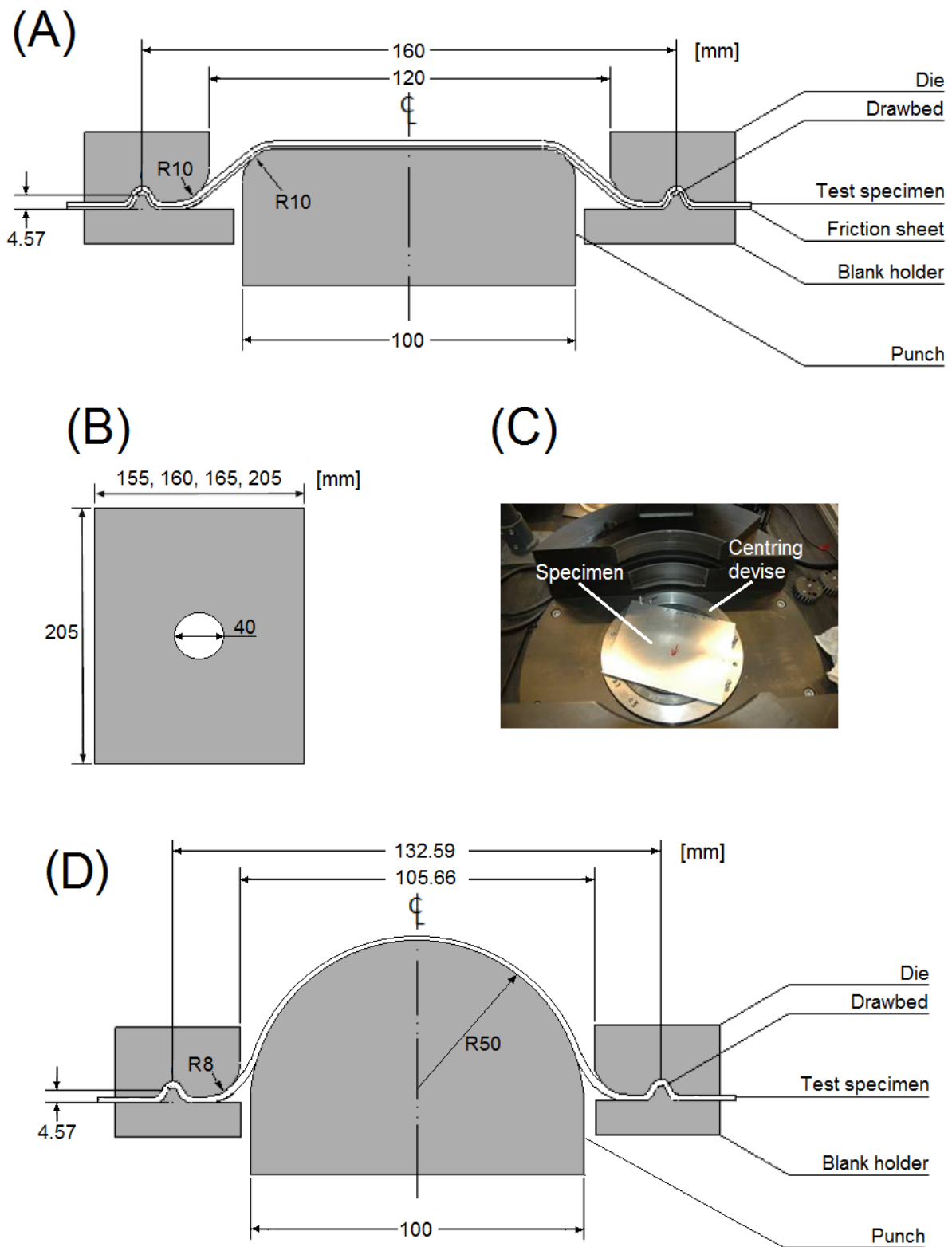
Fig. 3 (A) Marciniak-Kuczynski test set-up. (B) Marciniak-Kuczynski specimen dimensions (the hole is only for the friction sheet). (C) Centring devise used for the specimens. (D) Nakajima test set-up.
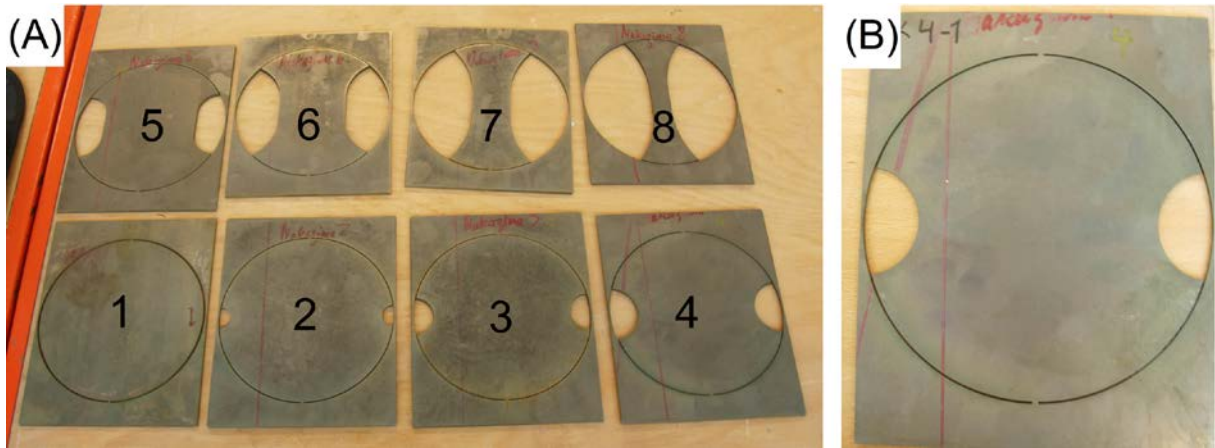
Fig. 4 (A) Nakajima test geometries, and (B) close-up of a specimen attached to the rectangular blank.
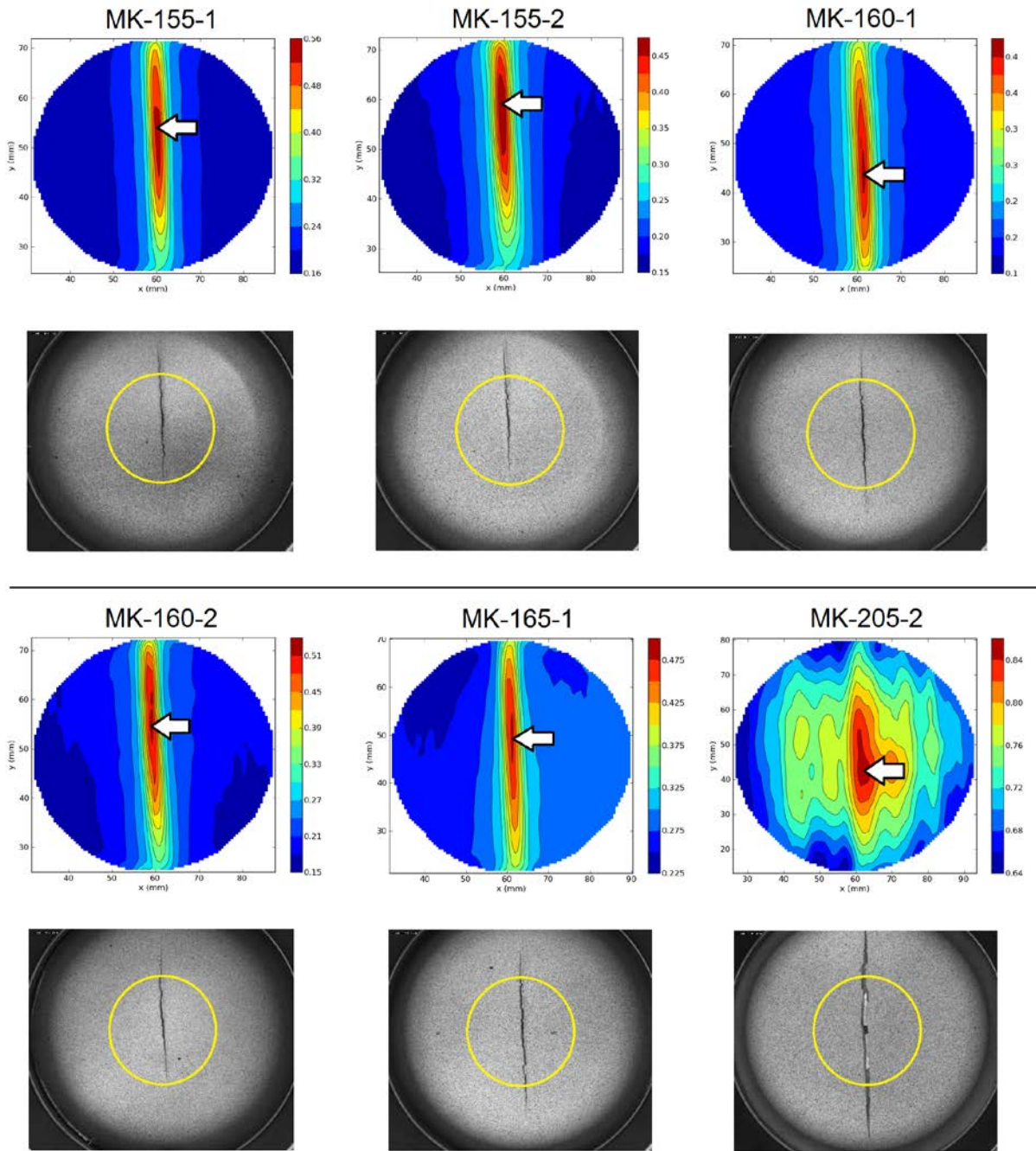
Fig. 5 Effective logarithmic strain in the last frame before fracture in the Marciniak-Kuczynski tests, and specimens after fracture. The arrows show where the deformation histories are collected, while the circles display the zones where the DIC measurements were applied.
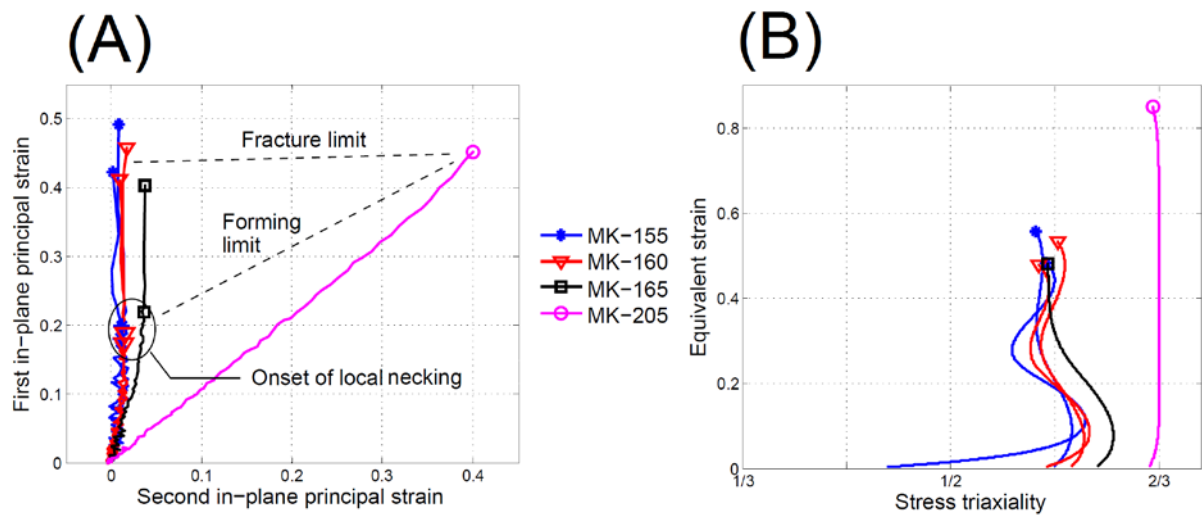
Fig. 6 Results from Marciniak-Kuczynski tests. (A) Principal in-plane logarithmic strains and (B) equivalent strain as function of stress triaxiality. The onset of local necking is displayed in (A) as well as the estimated forming limit and fracture limit curves.
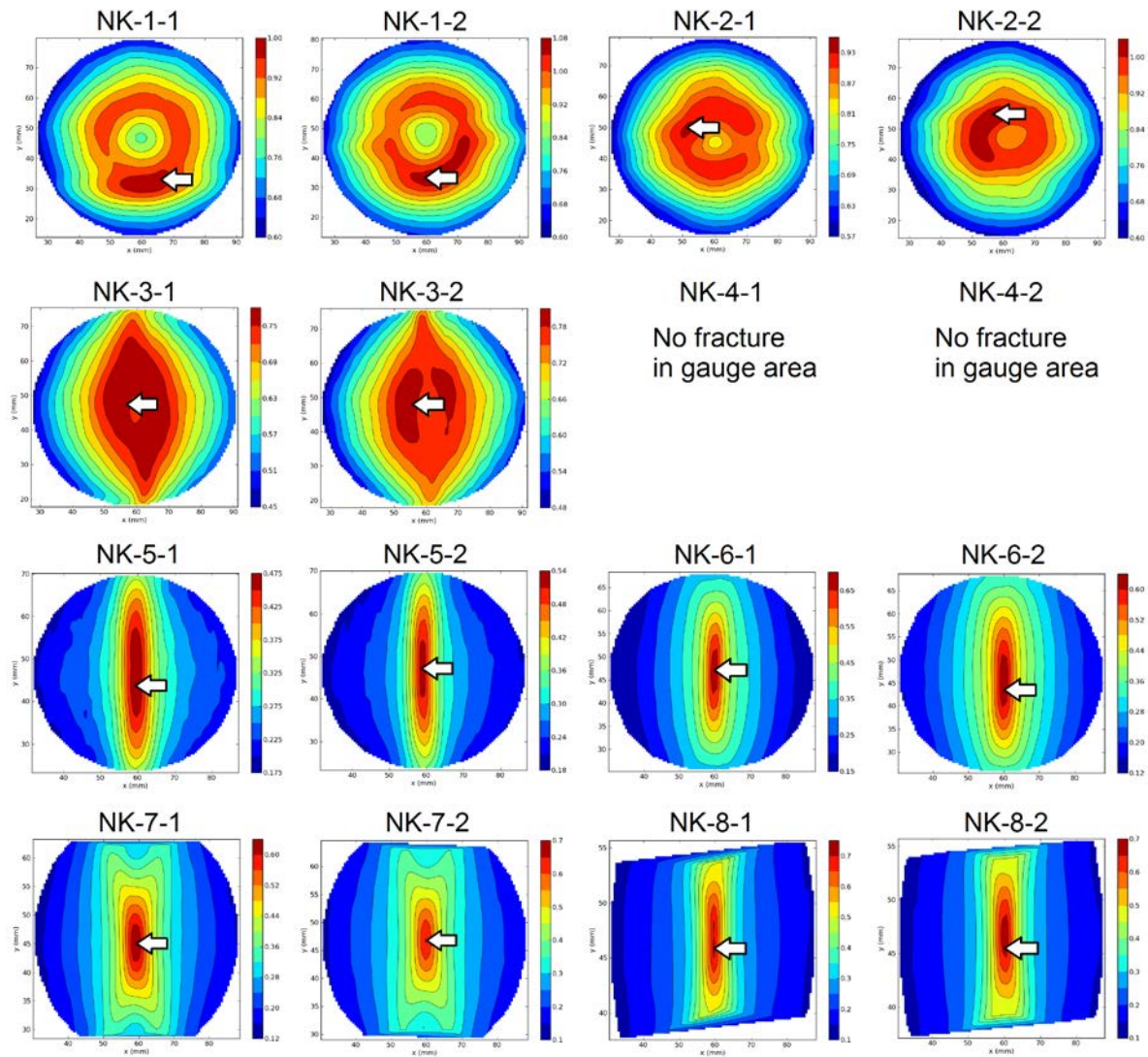
Fig. 7   Effective logarithmic strain in the last image before fracture in the Nakajima tests. The arrows show where the deformation values are collected.
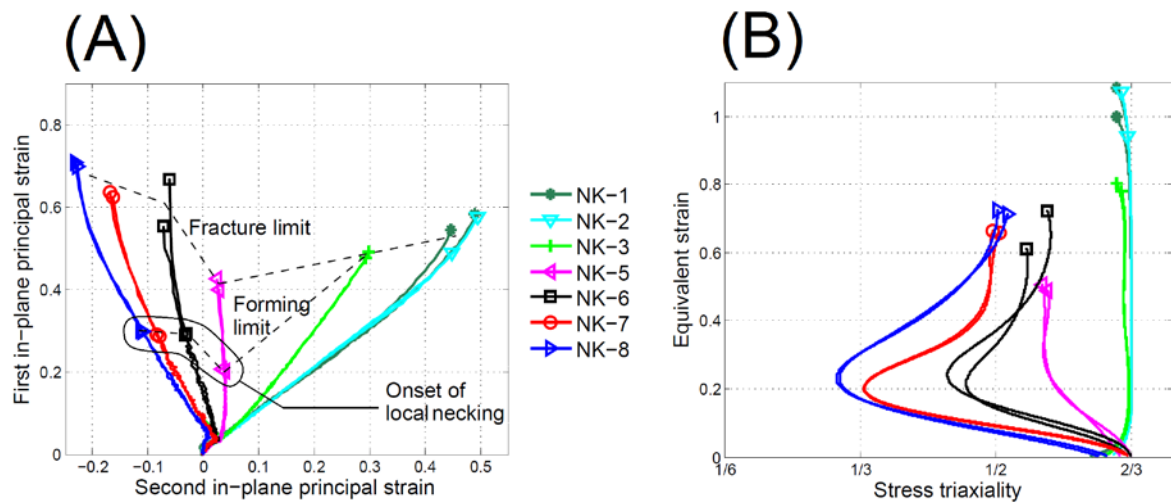
Fig. 8 Results from Nakajima tests. (A) Principal in-plane logarithmic strains, and (B) equivalent strain as function of stress triaxiality. The onset of local necking is displayed in (A) as well as the estimated forming limit and fracture limit curves.
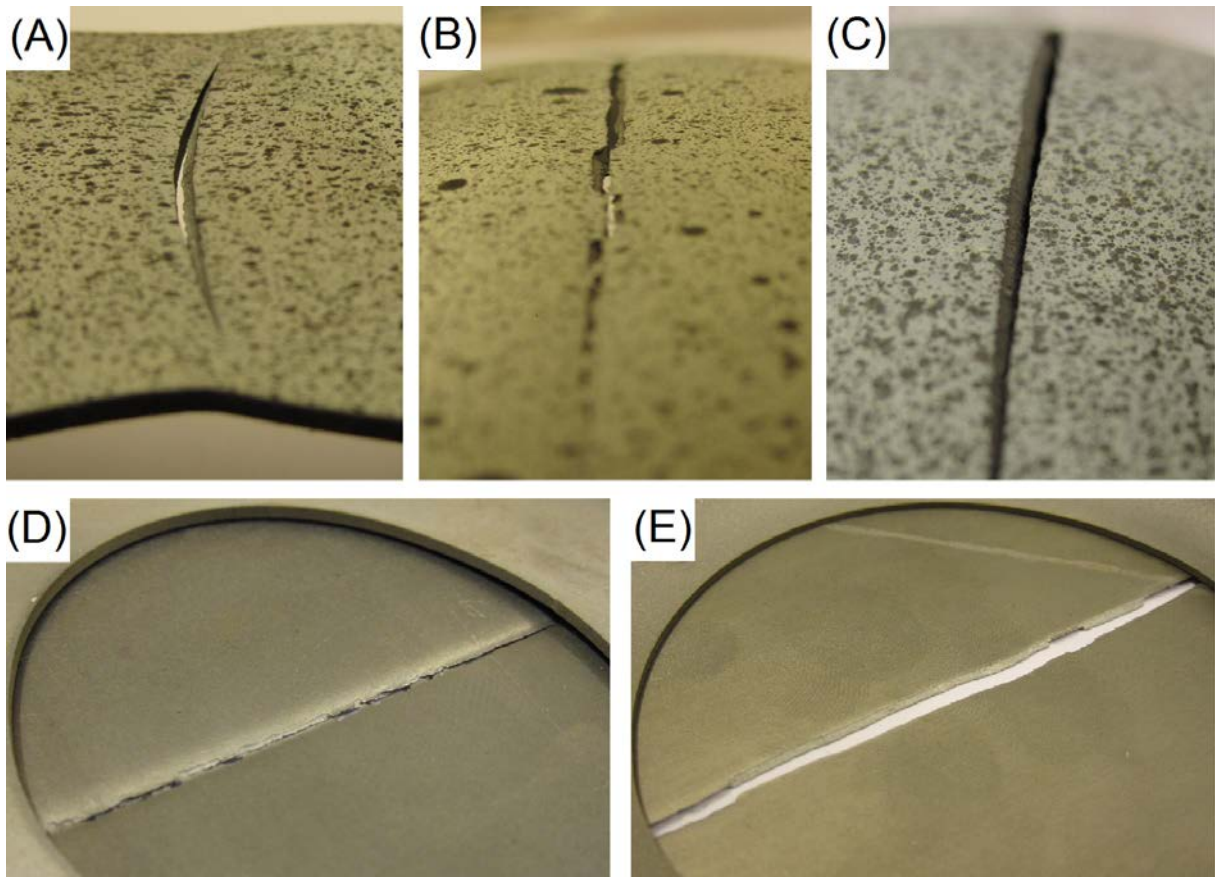
Fig. 9 Necking and fracture of selected tests. (A) NK-8-2, uniaxial tension, with diffuse and local necking, (B) NK-5-1, plane-strain tension, with local neck, (C), NK-1-1, equi-biaxial tension, and no necking, (D) MK-155-1, plane-strain tension, with local necking and (E) MK-205-2, equi-biaxial tension, with no necking.

25
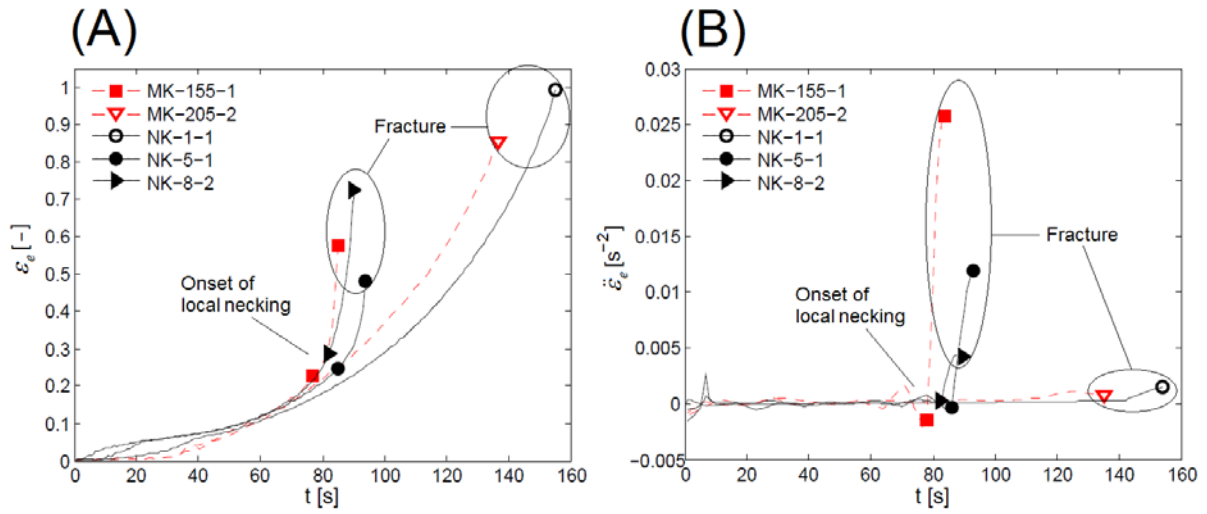
Fig. 10 Plots of (A) $\varepsilon_e(t)$ and (B) $\ddot{\varepsilon}_e(t)$ curves for selected tests. MK-155-1, NK-5-1 and NK-8-2, display an abrupt change in $\ddot{\varepsilon}_e$ due to local necking, while the MK-205-2 and NK-1-1 tests do not exhibit local necking, and thus the forming limit of these tests are governed by fracture.
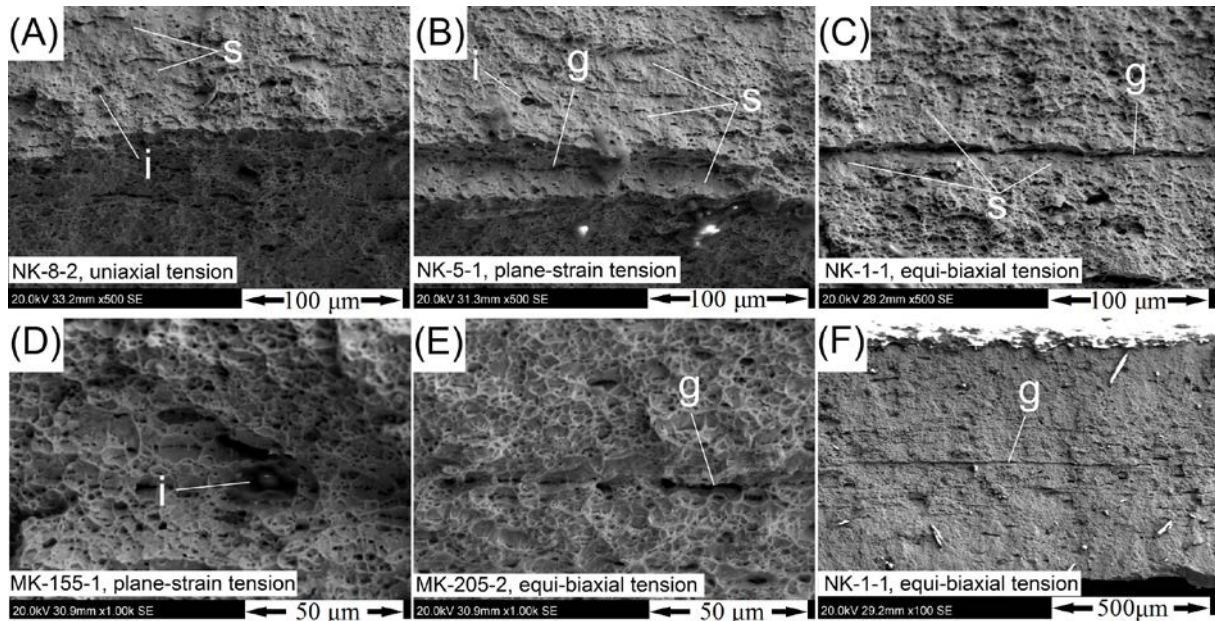
Fig. 11 (A-E) High magnification SEM fractographs of selected Nakajima and Marciniak-Kuczynski tests and (F) NK-1-1 at a lower magnification. 's' indicates some typical areas with shear fracture, while 'i' marks inclusions, and 'g' shows grooves found on the surface in three of the tests.
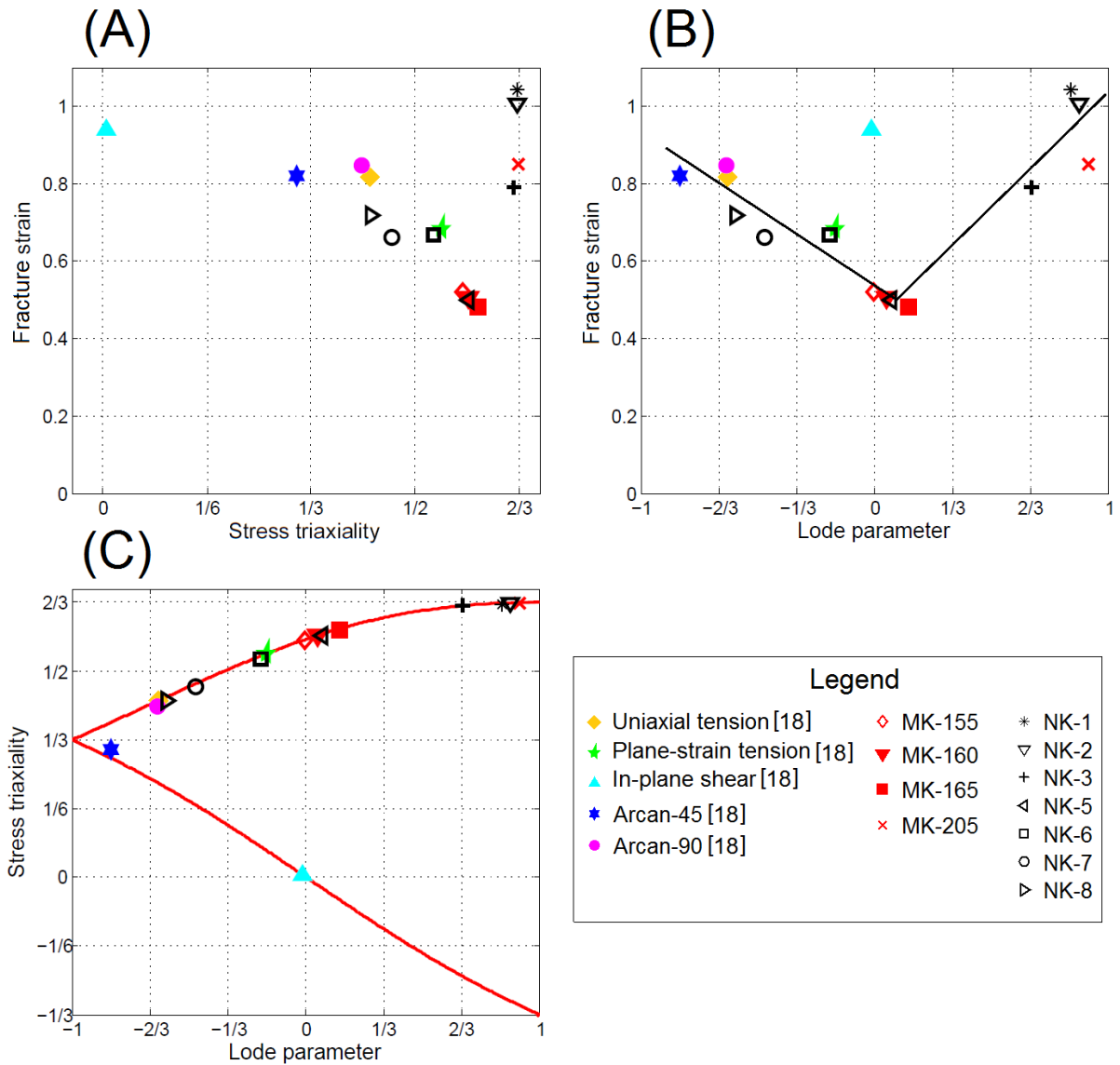
Fig. 12 (A) Fracture strain as function of average stress triaxiality. (B) Fracture strain as function of average Lode parameter, a trend line for the tests with $\sigma_{avg}^* > 1/3$ is marked. (C) Average stress triaxiality versus average Lode parameter for the various tests compared to the plane stress locus.